

Nonlinear EM-based Signal Processing

Mattia Fabiani^{*†}, Giulia Torcolacci^{*†}, Davide Dardari^{*†},

^{*} DEI, University of Bologna, 40136 Bologna, Italy

[†] National Laboratory of Wireless Communications (WiLab), CNIT, 40136 Bologna, Italy

Abstract—The use of high-frequency bands, combined with antenna arrays containing an extremely large number of elements (XL-MIMO), is pushing current technology to its limits in terms of hardware complexity, latency, and power consumption. A promising approach to achieving scalable and sustainable solutions is to shift part of the signal processing directly into the electromagnetic (EM) domain. In this paper, we investigate novel architectures that harness the interaction of reconfigurable passive linear and nonlinear (NL) scattering elements positioned in the reactive near field of signal sources. The objective is to enable multifunctional linear and NL EM signal processing to occur directly “over-the-air.” Numerical results highlight the potential to significantly reduce both system complexity and the number of RF chains, while still achieving key performance metrics in applications such as direction-of-arrival and position estimation, without the need for additional analog or digital processing.

Index Terms—NL-SIM, nonlinear, near-field, localization

I. INTRODUCTION

FUTURE 6th generation (6G) wireless networks, expected to support extreme data rates, ultra-low latency, and high reliability, will require a fundamental paradigm shift in physical-layer design [1]. Meeting these requirements calls for higher carrier frequencies and electrically large antenna apertures capable of fine electromagnetic (EM)-field control. The resulting increase in antenna elements and bandwidth naturally drives operation in the radiative near-field, where spherical wavefronts must be explicitly taken into account. At the same time, the scale of these arrays pushes the analog-digital interface closer to the antenna to limit losses and noise, demanding high-rate analog-to-digital converters (ADCs) and numerous radio-frequency (RF) chains. This configuration imposes a substantial digital burden, commonly referred to as the “digital bottleneck”.

Within this context, the emerging paradigm of electromagnetic signal processing (ESP) has attracted significant attention [2]. ESP proposes manipulating wireless signals directly at the EM level, i.e., *over-the-air*, using reconfigurable scattering structures operating passively to shape the EM field before digital conversion, thus exploiting the full degrees of freedom (DOF) offered by the wireless channel. Notably, these over-the-air transformations operate

at the speed of light with minimal active circuitry, enabling low-latency, energy-efficient implementations of key signal processing functions such as beamforming and spatial multiplexing [3].

Several architectures have been investigated as promising candidates for practical ESP implementations. Among them, stacked intelligent metasurfaces (SIMs) emerged as a hardware platform to enable ESP-based transceivers. A SIM consists of multiple stacked metasurface layers enclosed in a vacuum box, each comprising reconfigurable cells applying tunable phase shifts to the incident EM wavefront [4]. By operating according to the Huygens-Fresnel principle, each cell acts as a secondary radiating source, illuminating downstream layers and enabling a sequence of finely controllable interactions with the propagating EM field. This multilayer interplay provides continuous wave-domain processing, allowing SIMs to approximate a wide class of linear transformations with a fraction of the hardware complexity required by conventional antenna arrays. Although such linear operators are adequate for some wave-based tasks like beam steering and mode conversion, they inherently lack the expressive power required by parameter estimators and data-driven functionalities that depend on nonlinear (NL) mappings, e.g., physical-domain classifiers or analog neural operators (see, e.g., [5]). Prior attempts at RF-domain neural processing include [6], where a neural network (NN) is emulated using cascaded RF components; however, NL activations are implemented through an active feedback loop that requires continuous amplitude monitoring, limiting scalability and fully passive operation. Recent efforts toward NL metasurface-based processing include the nonlinear SIM (NL-SIM) architecture in [7], which introduces nonlinearity through a tunable step-type suppression mechanism. However, this approach is constrained to a specific thresholding mechanism, limiting its applicability to more general cell-level NL. In parallel, [8] proposes distributing neural computation across the wireless channel, but the NL activations are active, and the final combining is done in the digital domain, thus requiring a large number of RF chains.

Motivated by these limitations, we introduce a NL SIM architecture, termed NL-SIM, in which selected metasurface layers incorporate passive NL cells that apply pointwise NL transformations to the received EM field directly at RF. This configuration realizes an EM-domain analog of a NN, where conventional linear SIM layers exploit the EM superposition principle to realize linear transformations, while the NL cells act as activation functions, thereby enhancing the representational power of the structure for complex tasks such as near-field sensing and localization.

This work was partially supported by the European Union under the Italian National Recovery and Resilience Plan (NRRP) of NextGenerationEU, partnership on “Telecommunications of the Future” (PE00000001 - program “RESTART”), Structural Project S12 - Spoke 7, and by the EU Horizon project TIMES (Grant no. 101096307). Giulia Torcolacci was funded by an NRRP Ph.D. grant.

Building on this concept, we develop a general end-to-end EM transformation framework that rigorously captures the impact of element-wise NL and clarifies the constraints they impose on the equivalent low-pass model commonly used in the analysis of wireless systems. We further propose a practical circuit-level realization of the passive NL cell through a simple diode-based design, demonstrating its feasibility and physical consistency. Finally, by introducing a representative near-field localization use case, we show that NL-SIM achieves comparable performance whether the NL cell is fully trainable or controlled via fixed random biasing, offering clear advantages in terms of hardware simplicity and power consumption.

II. NL-SIM FOR NONLINEAR WAVE-BASED PROCESSING

The core premise of the proposed NL-SIM is to embed passive NL elements within the cells of one or more metasurface layers, thereby leveraging their intrinsic input-output NL relation to enrich the expressive power of the EM-level signals transformation and enhance the overall end-to-end learning capability. In this context, the NL-SIM can be conceptually viewed as an EM analog of a NN, but constrained by the physical laws governing waves propagation and cells' functioning. Leveraging this structural parallelism, the following analysis adopts standard terminology from the deep learning domain, including *training*, *bias*, and *inference*, to describe, respectively, the configuration, optimization, and operation of the physical device.

With reference to Fig. 1, the considered NL-SIM consists of a total number L of metasurface layers, where selected layers implement NL transformations and the remaining ones apply linear transformations. Denote by $\mathcal{L} = \{1, 2, \dots, L\}$ the set of indices corresponding to all the metasurface layers and by $\mathcal{Q} \subset \mathcal{L}$ the subset of cardinality Q of indices associated with the NL metasurface layers. Each layer comprises a square grid of M cells spaced by $\lambda/2$, with $\lambda = c/f_0$ denoting the wavelength at the carrier frequency f_0 , and c is the speed of light. In the case of linear metasurface layers, the transmission coefficient of the m th cells on the l th metasurface layer is represented by $\phi_m^{(l)} = e^{j\theta_m^{(l)}}$, with $\theta_m^{(l)} \in [0, 2\pi)$, for $m = 1, 2, \dots, M$ and $l \in \mathcal{L}$, and j denoting the imaginary unit. Therefore, the matrix of transmission coefficients for the l th metasurface layer can be expressed as $\Phi^{(l)} = \text{diag}(\phi_1^{(l)}, \phi_2^{(l)}, \dots, \phi_M^{(l)}) \in \mathbb{C}^{M \times M}$.

Let us consider a generic equivalent complex low-pass signal $\mathbf{s} \in \mathbb{C}^{M \times 1}$ associated with that impinging on the first metasurface layer of the SIM. The signal $\mathbf{x}^{(L)} \in \mathbb{C}^{M \times 1}$ at the output of the NL-SIM architecture can be obtained recursively as

$$\begin{cases} \mathbf{x}^{(0)} = \mathbf{s}, \\ \mathbf{x}^{(i)} = \begin{cases} \boldsymbol{\sigma}^{(i)}(\mathbf{W}^{(i)}\mathbf{x}^{(i-1)}) & , \quad i \in \mathcal{Q} \\ \Phi^{(i)}\mathbf{W}^{(i)}\mathbf{x}^{(i-1)} & , \quad \text{otherwise} \end{cases} \end{cases} \quad (1)$$

with $i \in \mathcal{L}$ and $\mathbf{W}^{(1)} = \mathbf{I}_M$. Here, the matrices $\mathbf{W}^{(l)} \in \mathbb{C}^{M \times M}$, $l \in \mathcal{L}$, model the propagation between the $(l-1)$ th and l th metasurface layer according to the Rayleigh-

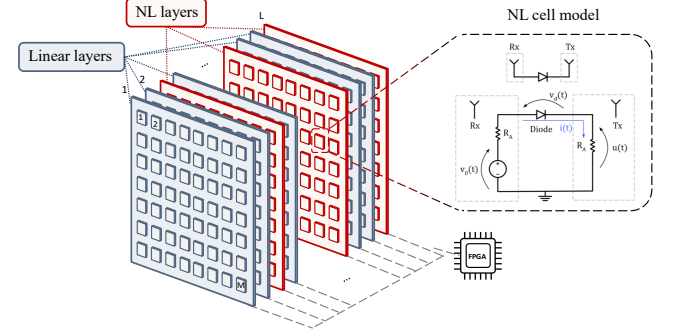


Figure 1. General NL-SIM architecture for wave-based signal processing.

Sommerfeld diffraction theory [4], whose (m, i) th entry is given by

$$[\mathbf{W}^{(l)}]_{m,i} = \frac{A \cos \chi_{m,i}^{(l)}}{d_{m,i}^{(l)}} \left(\frac{1}{2\pi d_{m,i}^{(l)}} - \frac{j}{\lambda} \right) e^{jk d_{m,i}^{(l)}}, \quad (2)$$

with $k = 2\pi/\lambda$ being the wavenumber, $d_{m,i}^{(l)}$ representing the propagation distance between the i th cell of the $(l-1)$ th layer and the m th cell of the l th layer, $\chi_{m,i}^{(l)}$ denotes the angle between the propagation direction and the cell's normal, while $A = \lambda^2/4$ is the area of each cell.

In addition, $\boldsymbol{\sigma}^{(i)} = [\sigma_1^{(i)}(\cdot), \dots, \sigma_m^{(i)}(\cdot), \dots, \sigma_M^{(i)}(\cdot)] \in \mathbb{C}^{M \times 1}$, $i \in \mathcal{Q}$, represents the vector of NL responses applied by each cell of the i th NL layer to the impinging EM signal. In general, the set of admissible NL activation functions cannot be selected arbitrarily. First, they must comply with the standard conditions required by the universal approximation theorem [9] (e.g., the activation must not degenerate into a purely polynomial function). Second, as the processing is performed over the air (i.e., at RF), the effective NL response in the low-pass equivalent representation deviates from that obtained at RF; hence, the physically implemented NL activation may induce a different complex low-pass behavior, as further detailed in the following section.

III. NONLINEARITIES MODELLING AT RF

In this section, we first clarify the link between the RF (i.e., bandpass) NL response and its low-pass equivalent representation. We then introduce two diode-based implementations of the NL cell. The resulting NL behavior can be either trainable or fixed: in the trainable case, the diode structure is unchanged and its operating point is optimized during learning, whereas in the fixed case the operating point is predetermined and diversity is introduced by randomly sampling the diode doping parameter.

A. Nonlinearity: Bandpass vs. Low-pass

Consider a generically modulated narrowband RF signal $s(t) = V(t) \cos(2\pi f_0 t + \phi(t))$, with $V(t) \geq 0$, and its equivalent complex low-pass representation $x(t) = V(t) e^{j\phi(t)}$. Suppose the signal passes through a memoryless NL device exhibiting a bandpass response $u(t) = F[s(t)]$, followed by

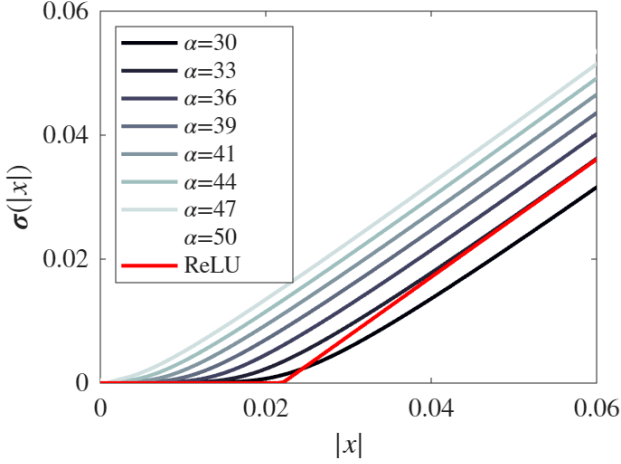


Figure 2. Examples of NL activation functions having a common bias voltage of $b = 0.4$ V for varying α values. The ReLU approximation for the $\alpha = 33$ case is reported in red.

a zonal filter eliminating all the harmonic components except the fundamental at f_0 . Denote with $y(t)$ the complex low-pass version of the resulting filtered output $\tilde{u}(t)$. The following theorem holds

Theorem III.1. *The NL relationship between $y(t)$ and $x(t)$ is given by*

$$y(t) = \sigma(x(t)) = C[|x(t)|] e^{j \arg\{x(t)\}}, \quad (3)$$

where the NL function $C[v]$ is given by

$$C[v] = \frac{2}{\pi} \int_0^\pi F[v \cos(\phi)] \cos(\phi) d\phi. \quad (4)$$

From (3), it follows that the equivalent low-pass response is governed by a NL relationship, which is in general different from that at RF $F[v]$. Moreover, the following properties hold: (i) only the amplitude of the input signal is affected by the NL, whereas the argument is unchanged; (ii) if $F[v]$ is an even function, then $C[v] = 0$ and the output is zero.

In the following, we report explicit expressions for $C[v]$ for some common NL functions $F[v]$. Specifically:

- $F[v] = \max(v, 0)$ (ReLU): $C[v] = v/2$ (Linear response)
- $F[v] = \max(v + a, 0)$ (Shifted ReLU):

$$C[v] = \begin{cases} \frac{1 + \operatorname{sgn} a}{2} v, & v < |a|, \\ \frac{1}{\pi} \left(v \arccos\left(-\frac{a}{v}\right) + \frac{a\sqrt{v^2 - a^2}}{v} \right), & v > |a|. \end{cases}$$

- $F[v] = |v|$: $C[v] = 0 \Rightarrow$ No output (even function).
- $F[v] = \operatorname{sgn}(v)$: $C[v] = \frac{4}{\pi} \Rightarrow$ Constant amplitude output.
- $F[v] = v^n$: $C[v] = \frac{\Gamma(1 + \frac{n}{2})}{\sqrt{\pi} \Gamma(\frac{3+n}{2})} = \frac{1}{2^n} \left(\frac{n+1}{2} \right)$, for n odd and zero otherwise, where $\Gamma[x]$ denotes the Euler gamma function [10].

B. Example of RF Nonlinear Activation

As a simple illustrative example, consider a practical NL activation cell in which a receive antenna is connected to a

transmit antenna on the opposite side of the surface via a diode, as shown in the inset of Fig. 1. In the same figure, the corresponding equivalent circuit for resonant antennas at frequency f_0 (e.g., half-wave dipoles) is also reported, where R_A denotes the antenna radiation resistance, $v_0(t)$ the open-circuit voltage of the receiving antenna induced by the impinging signal, $i(t)$ the current flowing in the circuit, and $v_d(t)$ the voltage across the diode.¹

The NL current-voltage characteristic of a diode is given by

$$i(t) = I_s \left(e^{\alpha v_d(t)} - 1 \right), \quad (5)$$

where I_s is the diode's saturation current and α depends on the thermal voltage and diode fabrication characteristics. The zonal filter is omitted, as the antenna itself acts as a filter for higher harmonics.

Denoting by P_a the available power of $s(t)$ (and thus $x(t)$) at the input antenna, i.e., the power that would be delivered to a perfectly matched load, it follows that $P_a = \mathbb{E}\{v_0(t)\}^2 / (4R_A)$ and $v_0(t) = 2s(t)$, where $\mathbb{E}\{\cdot\}$ represents the statistical expectation. The (unfiltered) transmitted signal corresponds to the voltage across the transmit antenna, i.e., $u(t) = R_A i(t)$. Therefore, the NL input-output relationship $F[\cdot]$ can be obtained by analyzing the circuit in Fig. 1, which is governed by the following transcendental equation

$$u(t) = R_A I_s \left(e^{\alpha 2(s(t) - u(t))} - 1 \right). \quad (6)$$

The solution of (6) and (4) can be evaluated numerically and possibly approximated with an analytically tractable expression, thus obtaining the cell's activation function $\sigma(x)$ in (3). In order to enhance the approximation capability of the NL-SIM, the activation functions must vary cell-by-cell. To this purpose, we consider two implementation paradigms:

1) *Trainable NL cells*: In the trainable configuration, the diode-based m th cell of the i th layer is fixed, but its operating point is optimized during training by adding a bias $b_m^{(i)} \leq 0$ to the input signal, which shifts the diode's current-voltage curve, hence modifying the shape of the induced NL activation. In this case, $\sigma_m^{(i)}(x)$ in (1) is given by $\sigma_m^{(i)}(x) = \sigma(x + b_m^{(i)})$. During the learning phase, each cell in the NL layer(s) adapts its bias so that the resulting NL extracts relevant features from the incoming signal. This can be physically implemented by embedding a controllable bias network within each cell or group of cells.

2) *Static random NL cells*: In the non-trainable case, the operating point is fixed for all elements, and no bias tuning occurs during learning. Instead, diversity is introduced at fabrication time by sampling the diode parameters such as α (e.g., doping concentration or junction area) from a predefined distribution. This yields a set of static NL activation curves $\sigma_m^{(i)}(x) = \sigma_{\alpha_{m,i}}(x)$, each slightly shifted horizontally due to manufacturing variations, where $\sigma_{\alpha_{m,i}}$ is obtained by solving (6) with parameter $\alpha = \alpha_{m,i}$ randomly chosen within a certain interval $[\alpha_{\min}, \alpha_{\max}]$. This approach is particularly appealing

¹The reactive elements of the equivalent circuit are omitted, as they are assumed to be counterbalanced through complex-conjugate impedance matching.

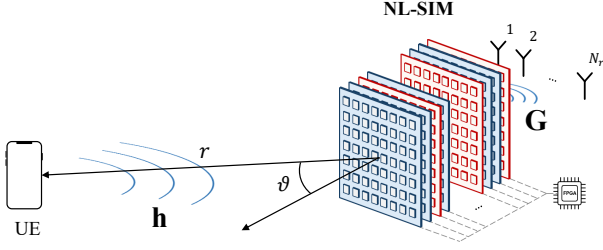


Figure 3. Considered scenario incorporating the proposed NL-SIM architecture for localization tasks in the near-field.

for fully passive deployments, as it avoids active biasing networks and reduces implementation costs while still enabling NL wave processing, as demonstrated in the numerical study.

In this regard, Fig. 2 shows several NL activation functions corresponding to different α values. As illustrated, varying α results in distinct NL responses. For numerical efficiency, each curve is approximated using a ReLU function in the simulations, without significantly affecting the overall behavior.

IV. USE CASE: NEAR-FIELD LOCALIZATION

This section illustrates a representative application of the proposed NL-SIM architecture for near-field localization. Let us consider the scenario depicted in Fig. 3, where a single-antenna user equipment (UE) transmits a narrowband pilot symbol $s \in \mathbb{C}$ toward the NL-SIM-based receiver. The receiving architecture comprises a NL-SIM followed by an uniform linear array (ULA) with N_R antenna elements, which is located at a distance d from the last NL-SIM layer. The UE is located in the radiative near-field region of the receiver, specifically at a distance $r \approx 0.1d_F$ from the receiver, being $d_F = 2D^2/\lambda$ the Fraunhofer distance [11]. The goal is to estimate the UE position instantaneously from its uplink pilot by leveraging the intrinsic wavefront curvature in the near-field, using a minimal number of RF chains and offloading part of the conventional baseband processing to the NL-SIM.

We define a Cartesian coordinate system centered in the first NL-SIM layer center. The UE position is given by the polar coordinates (r, θ) , where r denotes the radial distance from the NL-SIM aperture center, and θ represents the azimuth angle relative to the SIM aperture boresight (broadside direction). The near-field array response vector $\mathbf{a}(r, \theta) \in \mathbb{C}^{M \times 1}$ is expressed as

$$\mathbf{a}(r, \theta) = \frac{1}{\sqrt{M}} \left[1, \dots, e^{-jk(r-r_m)}, \dots, e^{-jk(r-r_{M-1})} \right]^T, \quad (7)$$

where r_m represents the Euclidean distance between the m th cell of the first layer and the UE. Furthermore, the near-field channel $\mathbf{h} \in \mathbb{C}^{M \times 1}$ between the UE and the SIM input layer is modeled as a Rician fading channel vector according to

$$\mathbf{h} = \frac{1}{\sqrt{P_L}} \left(\sqrt{\frac{\kappa}{\kappa+1}} \mathbf{a}(r, \theta) e^{j\gamma} + \sqrt{\frac{1}{\kappa+1}} \mathbf{h}_{\text{NLoS}} \right), \quad (8)$$

where P_L denotes the path loss, κ is the Rician factor, and $\gamma \sim \mathcal{U}[0, 2\pi)$ denotes a random initial phase. Moreover, \mathbf{h}_{NLoS} represents the non-line-of-sight (NLoS) component, capturing scattering effects, and is modelled as a Rayleigh fading vector with entries independently drawn from $\mathcal{CN}(0, \frac{1}{M})$.

To perform wave-domain localization, the NL-SIM processes the incident EM field layer-by-layer. Let us define the signal impinging on the input NL-SIM layer as

$$\mathbf{s} = \mathbf{h}s + \mathbf{n}, \quad (9)$$

where $\mathbf{n} \in \mathbb{C}^{M \times 1}$, $\mathbf{n} \sim \mathcal{CN}(0, \sigma_N^2)$, is the complex additive white Gaussian noise (AWGN) vector. Such signal then propagates through the L NL-SIM layers according to (1). Therefore, the signal $\mathbf{y} \in \mathbb{C}^{N_R \times 1}$ that is received at the ULA is given by

$$\mathbf{y} = \mathbf{G}\mathbf{x}^{(L)}, \quad (10)$$

where $\mathbf{G} \in \mathbb{C}^{N_R \times M}$ denotes the channel between the last NL-SIM layer and the receiving ULA, whose elements can be obtained by replacing $d_{m,i}^{(l)}$ in (2) with the distance between the each ULA element and the m th cell of the last NL-SIM layer.

Notably, the NL-SIM is engineered to extract the dominant near-field features, allowing the ULA to operate with simple amplitude-only measurements. The NL-SIM is thus trained to perform a physical regression task, mapping the received signal magnitudes directly to the UE position parameters (r, θ) . Specifically, for $N_R = 2$, this mapping reduces to

$$\begin{cases} \hat{r} = r_{\min} + \beta |y_1| (r_{\max} - r_{\min}), \\ \hat{\theta} = (2\beta |y_2| - 1) \frac{\pi}{2}, \end{cases} \quad (11)$$

where $[r_{\min}, r_{\max}]$ denotes the spatial range of interest, and β is a constant scaling factor such that $\beta \max(|y_i|) \approx 1, i \in \{1, 2\}$. The NL-SIM is explicitly trained to focus the signal onto each output antenna so that the measured amplitudes $|y_1|$ and $|y_2|$ provide a direct, linear indication of the corresponding target's range and angle parameters, respectively. Finally, the estimated UE position is recovered as $\hat{\mathbf{p}} = [\hat{r} \cos \hat{\theta}, \hat{r} \sin \hat{\theta}]$, which is the only operation performed in the digital domain.

V. NUMERICAL RESULTS

We hereby assess the performance of NL-SIM-based processing in terms of positioning accuracy, comparing it to a standard linear SIM to highlight the gains of NL wave-based operations. Comparisons with fully-digital schemes further illustrate that NL-SIM achieves competitive accuracy with substantially lower hardware complexity.

A. Simulation Setup

We generate a synthetic dataset of $N = 10^4$ channel realizations, assuming a carrier frequency of $f_0 = 28$ GHz. The UE positions are sampled uniformly in the near-field region, with radial distances $r \in [1, 3]$ m and azimuth angles $\theta \in [-70^\circ, 70^\circ]$, ensuring an even spatial coverage. The channel follows a Rician fading model with factor $\kappa = 20$ dB.

The transmit power is set to $P_T = 30$ dBm, while the receiver noise power is $\sigma_N^2 = -110$ dBm.

The considered receiving architecture comprises a ULA with $N_R = 2$ antenna elements and, unless otherwise stated, a NL-SIM with a total number $L = 6$ of metasurface layers. Each layer consists of $M = 1600$ cells arranged as a 40×40 square grid. The distance between the last NL-SIM layer and the ULA is set to $d = 3\lambda$. To stabilize training, i.e., bounding the magnitude of the backpropagated error gradients, the range and angle ground-truth are scaled to the range $[-1, 1]$ via

$$\begin{cases} r' = \frac{r - r_{\min}}{r_{\max} - r_{\min}} \cdot 2 - 1, \\ \theta' = \frac{2\theta}{\pi}. \end{cases} \quad (12)$$

The dataset is split into training, validation, and test sets, comprising, respectively, 80%, 10%, and 10% of the total dataset size N .

To update the NL-SIM weights during the training process, we utilize the root mean square error (RMSE) of the estimated UE position as the loss function. The RMSE also serves as a performance metric to assess positioning accuracy. Specifically, it is defined as

$$\text{RMSE} = \sqrt{\frac{1}{N_{\text{test}}} \sum_{i=1}^{N_{\text{test}}} \|\mathbf{p}_i - \hat{\mathbf{p}}_i\|^2}, \quad (13)$$

where $N_{\text{test}} = 0.1N$ is the test set size, \mathbf{p}_i is the ground-truth position vector, and $\hat{\mathbf{p}}_i$ is the position estimate.

All learning models are implemented in PyTorch. We leverage PyTorch's native support for automatic differentiation to calculate via backpropagation the gradient of the loss function with respect to the physical parameters, namely, the phase shifts $\Phi^{(i)}$ and the biases $b_m^{(i)}$. The SIM is trained using the Adam optimizer, treating the physical wave propagation as a differentiable forward pass. For comparison, the following architectures are evaluated:

1) **NL-SIM**: We consider a NL-SIM composed of L layers, where only one layer is equipped with NL activations, i.e., $Q = 1$. Specifically, for the static random NL cells, biases are first drawn from a standard Gaussian distribution, $b_m \sim \mathcal{N}(0, 1)$, then rectified and rescaled as $b_m \leftarrow -|b_m|/10^5$, shifting the NL curves to the right and producing a half-normal distribution with standard deviation 10^{-5} . Under the diode model of Fig. 2, this corresponds to the NL coefficient α approximately in the range $[55, 57]$. For trainable NL cells, α is initialized similarly but updated during training, while for static random cells the parameters remain fixed.

2) **Linear SIM**: In this case, the conventional linear SIM architecture with L layers is considered, whose unit-cells apply exclusively linear phase shifts (i.e., $Q = \emptyset$). This case allows isolating the performance gain specifically provided by the NL activation functions.

3) **Fully-Digital CNN**: A convolutional neural network (CNN) takes as input the raw baseband signal vector \mathbf{s} in (9) received at the NL-SIM side formatted as a $(\sqrt{M} \times \sqrt{M} \times 2)$ tensor, so that to embed both real and imaginary components. In particular, the CNN architecture consists of three stacked

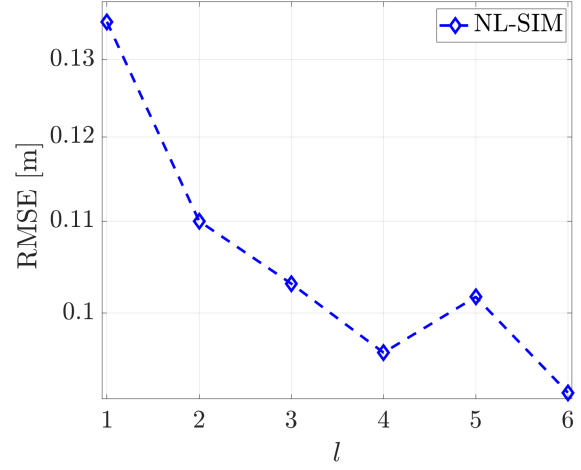


Figure 4. Position estimation RMSE as a function of the NL layer position l , $l \in \mathcal{L}$, for the case $L = 6$ and $Q = 1$.

convolutional blocks (namely, 2D Conv 3×3 , ReLU, Dropout with probability $p = 0.1$) followed first by a fully connected layer and then by a tanh activation function, which bounds the output to $[-1, 1]$; the estimated position is then obtained by inverting (12).

4) **Maximum Likelihood (ML)**: The maximum likelihood (ML) estimator is implemented as a grid-based exhaustive search, which serves as a performance lower bound. Given the received signal in (9) and the location-dependent array response vector $\mathbf{a}(r, \theta)$, the ML estimate is obtained by maximizing the beamforming gain (spatial matched filtering) over a discretized domain \mathcal{G} as

$$(\hat{r}, \hat{\theta})_{\text{ML}} = \arg \max_{(r, \theta) \in \mathcal{G}} |\mathbf{a}^H(r, \theta) \mathbf{y}|^2, \quad (14)$$

where $(\cdot)^H$ denotes the conjugate transpose. The grid \mathcal{G} is defined with resolution $N_\theta \times N_r$, with $N_r = N_\theta = 1000$, within the near-field region.

B. Impact of Non-Linear Layer Placement

First, we investigate the optimal NL-SIM architecture by analyzing how the placement of the NL activation layer influences localization accuracy. Specifically, we consider a NL-SIM in which the index $l \in \mathcal{L}$ (i.e., the layer position) of the NL layer is varied.

Fig. 4 shows the position estimation RMSE as a function of the NL layer index in the NL-SIM stack. The performance is highly sensitive to the placement of the NL processing, with the minimum RMSE achieved when the NL layer is applied at the final stage of the stack ($Q = \{L\}$). This observation aligns with standard NN design, where NL activations follow linear projection. Here, the preceding linear SIM layers collectively implement a linear matrix. Positioning the NL layer at the output enables it to act as a feature discriminator, shaping the final intensity distribution for accurate parameter readout. Conversely, placing NL earlier exposes the generated features to subsequent linear mixing, which attenuates the near-field

information essential for the amplitude-to-parameter mapping in (11). Based on this, we set $\mathcal{Q} = \{L\}$ for the subsequent evaluation.

C. Impact of Architecture Depth

We further evaluate the scalability of the proposed approach by varying the total number of SIM layers L . As shown in Fig. 5, increasing the architecture depth leads to a reduction in the RMSE for the NL-SIM case, whereas the linear SIM shows negligible improvement. Hence, a deeper SIM architecture offers a larger number of trainable parameters and more complex wave processing capabilities.

Notably, the performance of the NL-SIM with trainable biases is almost identical to the configuration with fixed random biases. This is a crucial finding from a hardware implementation perspective: it implies that complex active biasing circuits are not strictly necessary. Instead, as discussed in Sec. III, we can rely on fully passive diodes with a fixed bias term, significantly reducing power consumption and circuitry complexity without compromising accuracy.

However, a performance gap remains between the NL-SIM and the fully-digital systems. Compared to the SIM, the CNN achieves a lower RMSE since it processes the raw received digital signal without physical restrictions stemming from the specific hardware, hence applying unconstrained mathematical operations (e.g., arbitrary matrix multiplications), while requiring a fully digital implementation (1600 RF chains *vs.* 2 RF chains of the NL-SIM). In contrast, the SIM and NL-SIM computations are strictly limited by the laws of EM wave propagation, as per (2), and the specific metasurface geometry, which limits its generalization capabilities when compared to a software-based NN. Furthermore, the ML estimator attains the smallest localization error, i.e., approximately 8 mm, albeit at the cost of extremely high hardware complexity (1600 RF chains) or prohibitive computational search requirements. In contrast, the proposed NL-SIM achieves comparable accuracy with a one-shot estimation while substantially reducing the number of antenna elements.

VI. CONCLUSIONS

This work introduced the NL-SIM architecture by enriching stacked metasurfaces with passive NL cells, enabling multifunctional EM-domain signal processing. A rigorous EM-based framework was developed, capturing both inter-layer propagation and the constraints imposed by realistic RF NL responses, alongside the proposal of a simple diode-based implementation for passive NL operations.

The numerical study on near-field localization confirms the potential of this architecture. NL-SIM achieves accuracy comparable to far more complex fully digital front-ends while relying on a limited number of RF chains. The inclusion of NL provides a clear performance advantage over linear SIM, particularly when applied at the final layer, while deeper stacks further enhance accuracy. Interestingly, even static random NL cells perform close to fully trainable designs, indicating that effective low-power, passive implementations are feasible.

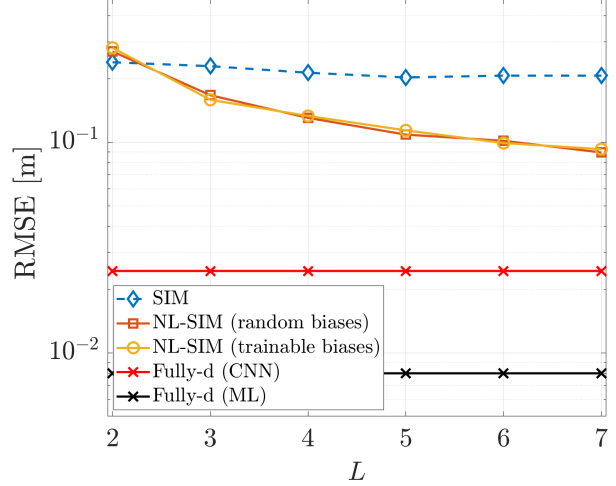


Figure 5. Position RMSE as a function of the total number of SIM layers L for $\mathcal{Q} = \{L\}$.

Overall, these findings demonstrate that embedding NL directly in the EM domain significantly increases the expressive power of metasurface-based receivers, enabling over-the-air regression tasks without additional analog or digital processing.

REFERENCES

- [1] International Telecommunication Union, "Framework and overall objectives of the future development of IMT for 2030 and beyond," Report M.2160-0, ITU-R, Geneva, Switzerland, Nov. 2023.
- [2] D. Dardari, G. Torcolacci, G. Pasolini, and N. Decarli, "An overview on over-the-air electromagnetic signal processing," *IEEE Signal Process. Mag.*, 2025, to appear.
- [3] D. Dardari, "Over-the-air multifunctional wideband electromagnetic signal processing using dynamic scattering arrays," *IEEE Trans. Wirel. Commun.*, pp. 1–1, 2025, to appear.
- [4] J. An, C. Xu, D. W. K. Ng, G. C. Alexandropoulos, C. Huang, C. Yuen, and L. Hanzo, "Stacked intelligent metasurfaces for efficient holographic MIMO communications in 6G," *IEEE J. Sel. Areas Commun.*, vol. 41, pp. 2380–2396, Aug. 2023.
- [5] Z. Gu, Q. Ma, X. Gao, J. W. You, and T. J. Cui, "Classification of metal handwritten digits based on microwave diffractive deep neural network," *Adv. Opt. Mater.*, vol. 12, p. 2301938, Oct. 2023.
- [6] X. Gao, Q. Ma, Z. Gu, W. Y. Cui, C. Liu, J. Zhang, and T. J. Cui, "Programmable surface plasmonic neural networks for microwave detection and processing," *Nat. Electron.*, vol. 6, pp. 319–328, Apr. 2023.
- [7] O. Abbas, A. Zayat, L. Markley, and A. Chaaban, "Nonlinear stacked intelligent surfaces for wireless systems," *arXiv preprint arXiv:2510.23780*, Oct. 2025.
- [8] K. Stylianopoulos and G. C. Alexandropoulos, "Universal approximation with XL MIMO systems: OTA classification via trainable analog combining," *arXiv preprint arXiv:2504.12758*, Sep. 2025.
- [9] M. Leshno, V. Y. Lin, A. Pinkus, and S. Schocken, "Multilayer feedforward networks with a nonpolynomial activation function can approximate any function," *Neural Netw.*, vol. 6, pp. 861–867, Mar. 1993.
- [10] A. Conti, D. Dardari, and V. Tralli, "On the analysis of single and multiple carrier WCDMA systems with polynomial nonlinearities," in *Proc. of ICICS-PCM 2003*, vol. 1, pp. 369–375, Dec. 2003.
- [11] C. A. Balanis, *Antenna Theory: Analysis and Design*. New Jersey, USA: Wiley, 2016.